Exsolved Ni nanoparticles acting as oxygen storage reservoirs and active sites for redox CH_4 conversion

Svenja-K. Otto[1], Kalliopi Kousi[2], Dragos Neagu[2]*, Leonidas Bekris[2], Jürgen Janek[1] & Ian S. Metcalfe[2]**

[1]Institute of Physical Chemistry & Center for Materials Research, Justus-Liebig-University Giessen, Heinrich-Buff-Ring 17, D-35392 Giessen, Germany, [2]School of Engineering, Newcastle University, Newcastle-upon-Tyne NE1 7RU, U.K.

KEYWORDS

Perovskites, exsolution, chemical looping, methane, hydrogen production, syngas

ABSTRACT

The growing demand for H_2 and syngas requires the development of new, more efficient processes and materials for their production, especially from CH_4 that is a widely available resource. One process that has recently received increased attention is chemical looping CH_4 partial oxidation, which however, poses stringent requirements on material design, including fast oxygen exchange and high storage capacity, high reactivity towards CH_4 activation and resistance to carbon deposition, often only met by composite materials. Here we design a catalytically active material for this process, based on exsolution from a porous titanate. The exsolved Ni particles act as both

oxygen storage centres and as active sites for CH_4 conversion under redox conditions. We control the extent of exsolution, particle size and population of Ni particles in order to tune the oxygen capacity, reactivity and stability of the system and, at the same time, obtain insights in parameters affecting and controlling exsolution.

Introduction

H_2 is an attractive, environmentally friendly energy carrier, while syngas is an important precursor for many industrial processes (Fischer-Tropsch). Consequently, new, more efficient routes for their production would be hugely beneficial[1,2]. Large scale production is dominated by catalytic CH_4 reforming; however, alternative processes like CH_4 conversion to syngas/H_2 through chemical looping (CL) are the subject of current research. In CL, a reaction is divided into multiple partial reactions, which are carried out separately, but are typically linked by a solid oxygen carrier material (OCM)[3]. This OCM is cycled between a reduction step, where CH_4 is oxidised by the lattice oxygen of a metal oxide (MO) and a subsequent oxidation step, where an O_2-containing stream replenishes the oxygen in the reduced oxygen carrier to revert it to the initial state as displayed below in Eq. 1 and 2. Separation of the two steps (and therefore reactants) in space or time eliminates side reactions and the need for product separation, which are required for catalytic CH_4 reforming[4].

$$CH_4 + MO \rightarrow CO + 2\ H_2 + M \quad \text{(Eq. 1)}$$
$$M + ½\ O_2 \rightarrow MO \quad \text{(Eq. 2)}$$

A suitable oxygen carrier material for this process has to fulfil several requirements, including high oxygen capacity and exchange rate, thermal and redox stability, as well as catalytic reactivity and resistance to carbon deposition[5–7]. So far, the state of the art catalyst for CH_4 reforming is Ni/Al_2O_3, which benefits from the strong catalytic properties of Ni towards CH_4 activation[8].

However, the material usually suffers from rapid deactivation through carbon deposition and metal sintering[9]. Previously reported ways to improve the catalytic activity of the materials include the tuning of the inert support[10–12], the incorporation of promoters such as alkali metal[13,14] or additional preparation steps[15,16]. So far, an ideal material for CL partial oxidation of CH_4 has not been identified. The most attractive oxygen carriers used are Mn and Fe oxides, although they all require far greater temperatures of around 900 °C to activate CH_4[7].

Exsolution could be a way to overcome the above material limitations. In this, confined, partly embedded nanoparticles are highly dispersed on the surface of supports through incorporation of the active, exsolvable metal species on the B-site of a perovskite and consequent segregation of the metal on the surface, which endows them with emergent functionality[17–20]. Particles prepared by redox exsolution have displayed enhanced activity, coking resistance and stability under hydrocarbon environments[21] and can additionally be tailored, which gives control over the properties of the resulting particles[22–24]. These characteristics combined with the fact that exsolution requires fewer preparation steps and less complex precursors would mitigate some of the risks associated with Ni based catalysts' toxicity.

In this study, we design and prepare a new perovskite system with exsolved Ni particles that fulfil the double role of oxygen storage reservoirs and catalytic centres and employ it towards redox conversion of CH_4 to H_2 via CL[25]. We show that by controlling the exsolution conditions, the amount, size and population of the exsolved nanoparticles can be tailored and directly linked to their oxygen capacity, reactivity and coke resistance. Additionally, this study provides new insight into the factors that control exsolution. Comparison with Ni-impregnated samples shows that our systems have superior resistance to coking, are more likely to fulfil the double role mentioned above and provide higher selectivity over syngas production.

Results and discussion

Perovskite design for redox conversion of CH_4

In order to prepare an exsolved system that exhibits, at the same time, high catalytic activity towards CH_4 activation and high oxygen capacity, it is necessary to control the extent of exsolution from the perovskite. The total amount of exsolved Ni, as well as particle size and population are of great importance because they are likely to dictate oxygen capacity, reactivity and stability against coking and agglomeration. Due to the known reactivity of Ni towards CH_4 conversion, we designed a material containing Ni^{2+} as the exsolvable B-site ion. We used a moderate substitution level of Ni^{2+} on the B-site (0.2, equivalent to ~6 wt% Ni) to be able to compare the exsolved material with conventional systems based on Ni/Al_2O_3 having similar loading. We then maximized the degree of Ni exsolution on the surface, to maximize oxygen capacity and reaction sites for CH_4 activation. A titanate lattice was chosen since it displays negligible oxygen capacity under redox conditions and would therefore isolate the Ni particles in their double role. Additionally, it would enhance the stability of the perovskite and thus preserve the confinement of the exsolved particles thereby enhancing their stability. A-site deficiency was incorporated in order to promote exsolution[22,26] and, at the same time, to create a stoichiometric residual perovskite after exsolution, which would prevent particle re-dissolution in the perovskite during oxidation[23]. For two key reasons it was also important to prepare the perovskite system in a porous microstructure, while still using a solid-state method which ensures control over stoichiometry. First, porosity would enable stability during cycling by better accommodating chemical expansion and contraction of the material under CL redox conditions. In addition, keeping in mind that exsolution of transition metals is generally limited to a region from under half a micron under the surface[21], a small grain size would also promote the formation of exsolved Ni particles as a higher surface area would be

available to exsolve from. Taking this into consideration, Ca^{2+} was incorporated on the A-site of the perovskite, in order to lower the perovskite formation temperature[27] and as a result, minimize the perovskite grain size and maximize the surface area. Also, the use of Ca^{2+} as an A-site ion promotes exsolution by facilitating oxygen anion and cation migration[21]. Furthermore, to promote oxygen anion transport, we adopt a perovskite stoichiometry that is slightly oxygen deficient, $\gamma = 0.05$. All the above considerations, together with the requirement of charge neutrality led to the design and preparation of $La_{0.5}Ca_{0.4}Ni_{0.2}Ti_{0.8}O_{3-\gamma}$.

According to the XRD analysis of the synthesized material, the phase corresponds to a single-phase perovskite despite the low sintering temperature (1100 °C for 12 h). The Rietveld refinement of the XRD pattern, presented in Fig 1a, shows good agreement between experimental and calculated data (*wR* value[28] of 5%) and reveals the crystal structure of the perovskite. Microstructural analysis of the prepared perovskite with SEM, Fig 1b, demonstrates that the perovskite is porous after sintering at 1100 °C with homogenous perovskite grain sizes of about 500 nm in diameter. Normally perovskites prepared with solid-state methods consist of much larger grains in the order of tens of microns[22]. The decreased grain size obtained by the modified solid-state method allows a high extent of exsolution and consequently high activity.

Controlling the extent of exsolution

In order to control the extent of exsolution and the particle population and size, the perovskite samples were reduced in H_2 at different temperatures between 700 °C and 1000 °C for 10 hours and, additionally, under CH_4 by heating to 750 °C (no dwell time). In order to evaluate the extent of exsolution and its impact on the perovskite crystal structure, phase analysis with XRD and subsequent Rietveld refinement were performed for the samples after reduction. The XRD pattern

of the samples reduced at different temperatures in H_2 are shown in Fig 2a. The reflections of the Ni phase, shown in detail for one reflection in Fig 2b, clearly become more intense with an increase in reduction temperature, indicating that the exsolved Ni phase fraction increases. Quantitative values obtained by refinement for the extent of exsolution (ξ, moles of Ni per moles of perovskite) and the pseudocubic perovskite unit cell parameter (a_P, Å) are plotted in Fig 2c. The fraction of Ni metal increases gradually with the reduction temperature, while the perovskite crystal structure is preserved. After in situ reduction with CH_4, the fraction of exsolved Ni (not shown in the plot) is almost identical to the one being exsolved at 700 °C under H_2, indicating that the reduction temperature and not the reducing gas or the reduction time is the important factor for controlling exsolution in this case.

Moreover, an Arrhenius plot of the extent of exsolution as a function of reduction temperature (Fig 2d), reveals that Ni exsolution from the prepared perovskite is a thermally activated process with an activation energy of about 45±4 kJ mol^{-1}. Interestingly, and contrary to expectations, this value is typical for oxygen ion diffusion in perovskites and much lower than the values generally reported for cation diffusion[29,30]. This seems to indicate that exsolution is actually controlled by oxygen ion diffusion within the perovskite structure rather than by cation transport. This is probably due to the fact that the designed perovskite is A-site deficient as A-site vacancies are known to facilitate B-site cation transport, but also probably due to the small perovskite grains prepared here which do not require Ni ion diffusion over long distances[31].

The evolution of the pseudocubic cell parameter (Fig2c) of the residual perovskite phase displays a nonlinear trend with respect to the reduction temperature and the extent of exsolution. Several factors are expected to influence the cell parameter during reduction, leading to the complex trend observed. Firstly, as oxygen leaves the perovskite structure during reduction, the perovskite is

doped with electrons and oxygen vacancies. Therefore, the oxidation state of the cations decreases, which leads to an expansion in unit cell volume[32]. Accordingly, the unit cell of the perovskite phase increased from the sintered to all reduced samples. At the same time, the exsolution process takes place and Ni^{2+} leaves the perovskite structure. As Ni^{2+} ions (0.69 Å) are bigger than Ti^{4+} ions (0.605 Å)[33], Ni exsolution counteracts the expansion of the cell. Both effects might have cancelled each other out for the samples reduced in situ and up to 900 °C, as a_P did not change significantly. Regarding the Ni phase fraction after reduction at 1000 °C, the value clearly exceeded 0.1, which is the A-site deficiency of the $La_{0.5}Ca_{0.4}Ni_{0.2}Ti_{0.8}O_{2.95}$ composition. Consequently, an A-site excess perovskite was created under these conditions. This is reflected by the pseudocubic parameter which increased considerably for the sample reduced at 1000 °C[34] as compared to the sample reduced at 900 °C.

Controlling particle size and population

Changing the reduction temperature did not only change the extent of exsolution but also allowed us to effectively control the size and population of the exsolved particles. SEM images of the perovskites after reduction under different conditions (Fig 3a) confirm, that all temperatures used in this study are suitable for Ni exsolution, thus, particle size and population were largely dependent on those temperatures.

SEM image analysis was performed to determine the values for particle average diameter size (s, nm) and population (P, number of particles μm^{-2}). It is obvious that the particle population decreases and the particle size increases monotonically with increasing reduction temperature, leading to an overall increase in the total number of Ni atoms exsolved (η_{Ni}, atoms μm^{-2}). This is consistent with the nucleation theory and previous reports on exsolution[22,35,36], indicating that

particle nucleation occurs at lower temperatures, while the particles grow in size at higher temperature. Our results indicate that for temperatures equal to or higher than 700 °C the reduction time or gas do not seem to kinetically limit exsolution. This is demonstrated by the fact that when exsolution is carried out at 700 °C, under CH_4 stream with no dwell time, or under H_2 stream for 10 or 30 h, very similar particle characteristics in terms of size and population were observed, confirming that for these samples it is mainly the temperature that mediates the exsolution process and not the time or the reducing gas (Fig 3b).

Probing the reactivity of exsolved systems for CH_4 conversion

In order to determine the impact of the extent of Ni exsolution and the particle properties of this system, we employed CH_4 activation experiments, and monitored CH_4 conversion and selectivity as a function of temperature (Fig 4a-i). These are used to probe the surface activity of the samples as well as their oxygen capacity[37,38]. For an as-prepared, i.e. not exsolved sample, conversion started at 520 °C and was low over the entire temperature range investigated, since the sample does not contain any exsolved Ni nanoparticles. The small amount of conversion observed is probably due to a limited oxygen capacity of the perovskite lattice. It should be noted that this experiment can be regarded as in situ reduction under CH_4 stream. Indeed, as observed by following SEM analysis, particles were exsolved during this experiment (Fig 3a). After that process, the material was oxidized and tested again to check the reactivity of the in situ produced particles. In this case, the system was capable of activating CH_4 starting at 500 °C, although the conversion and consequently the H_2 production were still quite low. Under these conditions the catalyst produced clearly more CO than CO_2, which is reflected in a gas phase selectivity to CO of about 85%. The MTPR activity after reduction in H_2 at 700 °C was comparable, which is not

surprising considering the similarity in the extent of exsolution as well as in particle size and population. For the sample reduced at 800 °C, the catalytic profile seems quite similar to the previous mentioned samples. However, it is worth noting that there is a shoulder in the H_2 signal, indicating the presence of an additional higher temperature activated process (Fig 4i). Also, reduction at higher temperatures causes the appearance of a third, additional peak of CH_4 conversion towards CO and H_2 at about 670 °C. These two additional peaks become more pronounced after further increase in the reduction temperature (850 °C and 875 °C), while the MTPR profile remains quite similar. More increase in the reduction temperature (900 °C) causes important changes in CH_4 conversion in what seems like a step change, which is probably caused by increasing the extent of exsolution up to the level of the A-site deficiency of the perovskite. The activation temperature decreased to 420 °C and two separate peaks corresponding to CO and CO_2 production were present in the CH_4 signal. They were followed by a third peak which corresponds to carbon deposition, as H_2 was the only gaseous product during this time. The high temperature additional CH_4 peak corresponding to CO and H_2 production was still present, but shifted to lower temperatures, which was identified as a general trend when increasing the reduction temperature. This might be assigned to a higher Ni surface coverage, a higher mobility of ions in the perovskite lattice or even a change in the interaction of the particles with the support. Reduction at 1000 °C produced a similar MTPR pattern with increased conversion but also more carbon deposition. It is worth noting that exsolved particles have been demonstrated before to display limited coking and although carbon deposition is present in this study, it still remains very minor in comparison to a material prepared conventionally by impregnation (see last section). Furthermore, the gas phase selectivity to CO versus CO_2 is 80% or higher for all exsolved perovskite samples, which would make them good candidates for syngas production. However,

overall it seems that the H_2/CO ratio is more than 2 which means that the decomposition of CH_4 dominates over the oxidation and that would make them more applicable to H_2 production processes.

Correlating the characteristics of exsolved systems with their reactivity

To correlate the discussed observations concerning the exsolution process, the reactivity for CH_4 activation and H_2 production (Fig 5a), a n-dimensional plot format is proposed (Fig 5b). The extent of exsolution correlates to the oxygen capacity and the overall CH_4 conversion, the latter being higher in absolute values because it sums up the ability of the samples in CH_4 reforming, as well as in cracking the reactant. Therefore, the extent of Ni exsolution is the important factor that unlocks the ability of these materials to store oxygen, while, at the same time, the Ni particles also act as CH_4 activation sites. Furthermore, the particle size seems to be the determining factor for carbon deposition, since larger nanoparticles, formed during reduction at higher temperature, are more prone to carbonaceous deposits than their smaller counterparts. This is not surprising, since it has been reported before that a decrease in Ni size makes materials less susceptible to coking[39–41]. The reason for this is, that the step edges of the Ni particles, being the preferential growth centers for carbon deposition, become too small for carbon nucleation, which in turn suppresses coking. Supporting this, SEM images after testing (Fig 5c) indicate that the small nanoparticles, which were formed through reduction at 700 °C, show no signs of carbon deposition after testing. For the particles exsolved at 875 °C, the formation of carbon fibres is also negligible. However, after reduction at 900 °C, carbon fibres attached to Ni particles were clearly present. This suggests that as the reduction temperature increases, the anchorage of nanoparticles on the support decreases, making them more prone to coking. This is possibly due to the use of Ca^{2+} on the A-

site of the perovskite which was used to promote exsolution but, which for higher reduction/exsolution temperatures, seems to be detrimental for the maintenance of a good anchorage of the formed particles to the perovskite support. Contrary to our expectations, the high population, small size particles formed at lower exsolution temperature did not appear to be more active in terms of low temperature CH_4 activation, which seems to be rather dominated by the extent of exsolution and consequently by the oxygen capacity of the material.

Comparison between exsolved and infiltrated samples

We compare our system (1.2 $m^2\ g^{-1}$) with exsolved Ni particles, on a weight basis against the same low surface area system but with impregnated Ni particles and against a high surface area (100 $m^2\ g^{-1}$) Ni/Al_2O_3, which is a reference material for various catalytic CH_4 transformations (~8 nm size). We choose to compare those to the $La_{0.5}Ca_{0.4}Ni_{0.2}Ti_{0.8}O_{3-\gamma}$ perovskite after exsolution at 875 °C, which showed the best combination of high CH_4 conversion and low carbon deposition during testing under CH_4 stream (Fig 6f). The microstructural analysis of the samples after reduction (Fig 6a-c) shows that the Ni is well dispersed on the porous alumina support. For the Ni-impregnated perovskite, the Ni particles are, with an average diameter of 44 nm, considerably larger than the exsolved ones.

For Ni/Al_2O_3 a high conversion was expected, because of the high Ni loading available on the surface (10 wt% versus approx. 3 wt% exsolved to the surface), compared to our exsolved perovskites. However, carbon deposition was very pronounced and the starting temperature for CH_4 activation was the highest of the three materials, despite the good dispersion (Fig 6d). For the impregnated sample, CH_4 activation temperature and MTPR conversion profile were at lower temperature very similar to the exsolved sample reduced at 1000 °C, even though the metal content

is double (6 wt%) (Fig 6e). This might indicate that indeed part of the Ni exsolved at higher temperatures is loosely anchored to the support and acts as if it was an infiltrated sample. In addition, the gas phase selectivity to CO is only about 55%. However, even for those samples the interaction with a perovskite support seems to be beneficial in terms of resistance against coking. To define the carbon deposition on those surfaces qualitatively (Fig 6g) and quantitatively (Fig 6h), oxidation of the surface carbon followed testing (OTPO experiments[42]). The Ni/Al_2O_3 sample deposited the most carbon on the surface even in comparison to the high particle size impregnated perovskite. For all three samples, CO_2 is detected above 400 °C. Surface carbonaceous species which are gasified at temperatures higher than 400 °C usually correspond to C^{γ} or graphitic carbon and their formation has been reported previously for Ni-catalysts exposed to CH_4 above 550 °C. The two perovskite samples show only one type of carbon, while three different types were detected for the Ni/Al_2O_3. Generally, it is known that the oxidation temperature increases with the degree of crystallization of the carbon. Therefore, the high temperature OTPO peak for Ni/Al_2O_3 possibly belongs to more crystalline C^{γ} [43,41]. The OTPO peak at lowest temperature could accordingly be originated from less crystalline carbon or from coke containing hydrogen[44,45]. In total, the well anchored exsolved nanoparticles after reduction at 875 °C provide the best selectivity ratio of the gas products CO_x to carbon deposition, essentially the selectivity to desired products, when compared to the other two impregnated samples (Fig 6i). Interestingly, even the impregnated perovskite has better performance than the Ni/Al_2O_3 which can be attributed to the interactions of the Ni particles with the highly mobile perovskite support.

Stability during redox cycling

In order to test the applicability of the system we test its stability and cyclability over multiple chemical looping cycles (Fig. 7a). We select the material reduced at 875 °C based on the considerations discussed above. We carry out cycling with various cycle lengths (1 and 5 min, Fig. 7b-e) at 550 °C, corresponding to the end of the temperature activity window identified above (Fig. 4f) and at 30 mL min^{-1} (NTP). The results show that the system is cyclable and does not seems to display signs of degradation with time on stream and cycling (see first and last 5 cycles of each experiment Fig. 7). Nanostructure analysis of the material at different stages of the process (after reduction, after TPO and stability Fig. 7f-h) show that particles generally maintain their size and position even after oxidation and multiple cycles. The above findings demonstrate that the materials designed here can be used for cyclable applications providing long term stability and high activity.

Conclusions

In this work, we design a porous perovskite, $La_{0.5}Ca_{0.4}Ni_{0.2}Ti_{0.8}O_{3-\gamma}$, capable of Ni exsolution and characterise its activity for CH_4 conversion in a chemical looping application. Through this choice of stoichiometry, it was possible to control the microstructure of the material in a way that was beneficial for promoting exsolution. Reduction of the material under different temperatures and conditions allowed us to tailor the extent of exsolution and the particle characteristics. Firstly, the amount of exsolved Ni increased linearly with the reduction temperature, while the perovskite lattice remained stable. Interestingly, the activation energy of the exsolution process matches well with the values reported for oxygen ion diffusion within perovskites, which consequently implies that the controlling factor for exsolution could be oxygen rather than cation transport. Additionally, employing XRD and SEM image analysis we show that neither the reducing gas nor the reduction

time are the determining factors for exsolution control in this case, but predominantly the reduction temperature, where the particle population decreased and the particle size increased with increasing reduction temperature. However, in contrast to the monotonic development of the particle properties with increasing reduction temperature, MTPR tests showed a step change in activity towards CH_4 conversion after reduction at 900 °C, for which the CH_4 activation temperature dropped while the coking increased importantly. Through evaluation of a n-dimensional plot of the determined properties, the extent of exsolution is directly connected to the oxygen capacity and the CH_4 conversion of the material. Furthermore, particle characteristics were found to influence the activation temperature and the selectivity, but also the socketing and therefore the coking resistance of the nanoparticles. Additionally, comparison with Ni-impregnated samples showed, that our systems have superior resistance to coking and provide higher selectivity for syngas production. When tested under redox cycling for more than 50 cycles the material seems to not display signs of degradation with the particles maintaining their position and size. Finally, the materials prepared in this study should display moderate electronic and ionic conductivity values characteristic of titanates which would make them applicable in other energy conversion technologies such as fuel electrodes in solid oxide fuel or electrolysis cells.

Experimental

Sample preparation

Perovskite Synthesis

A modified solid-state method was applied for the synthesis of the $La_{0.5}Ca_{0.4}Ni_{0.2}Ti_{0.8}O_{2.95}$ perovskite. The process is described in detail elsewhere[21]. La_2O_3 nanopowder (99%, Sigma-Aldrich Chemistry), $CaCO_3$ (99.95%, Alfa Aesar), $Ni(NO_3)_2 \cdot 6H_2O$ (98%, Alfa Aesar) and TiO_2 nanopowder (99.5%, Sigma-Aldrich Chemistry) were used as precursors. First, the oxide and carbonate precursors were dried ($CaCO_3$ and TiO_2 for 3 h at 400 °C; La_2O_3 for 3 h at 800 °C) and weighed while hot. Afterwards, the Ni nitrate and polymeric dispersant (Hypermer KD1-SO-(AP), CRODA) were added and the mixture was sonicated in acetone. After evaporating the acetone, the resulting powder was calcined at 1000 °C for 12 h, followed by ball-milling and subsequent sintering in pellet form at 1100 °C for 12 h. After sintering, the pellets were crushed and sieved to get powder with a particle size between 80 and 160 μm.

Processing

In order to populate the perovskite surface with exsolved nanoparticles, the sintered powder was reduced under a 100 mL min^{-1} gas flow of 5% H_2/He for 10 h. The reduction temperature was varied between 700 °C and 1000 °C in order to control the extent of exsolution and the particle properties. Reduction for 30 h at 700 °C was additionally conducted. Afterwards, the reduced samples were oxidised in air for 1 h at 600 °C. All heating and cooling rates were set to 5 °C min^{-1}.

Reference samples

For the preparation of the impregnated samples, 6 wt% Ni/$La_{0.4}Ca_{0.4}TiO_3$ and 6 wt% Ni/Al_2O_3, a commercial γ-Al_2O_3 (~100 m^2 g^{-1}) powder and a $La_{0.4}Ca_{0.4}TiO_3$ (prepared by modified solid-state method) were used as supports. The support was dispersed in a dilute aqueous solution of Ni nitrate under continuous stirring, followed by water evaporation and drying at 90 °C overnight. The dried material was submitted to temperature programmed calcination (10 °C min^{-1}); the final temperature was 500 °C with a dwell time of 4 h. After calcination, the material was sieved to the same size as above, 80-160 μm, and reduced under a continuous flow of 5% H_2/He (25 mL min^{-1}) at 900 °C for 4 h with heating and cooling rates of 5 °C min^{-1}.

Material characterisation

XRD analysis and Rietveld refinement

Room temperature XRD analysis in reflection mode was carried out for all samples before and after reduction, using a PANalytical X'Pert Pro Multipurpose diffractometer (MPD) equipped with an X'Celerator (Real Time Multiple Strip detector). For data processing the software programme Win XPOW was used. The theoretical pattern of a perovskite double cell with the space group $Pm\bar{3}m$ was calculated, to identify peaks originating from the perovskite and from secondary phases. Subsequent identification of secondary phases was done with HighScore Plus.

To quantify the fraction of the secondary phases and to further evaluate the perovskite phase, Rietveld refinement was done with the software programme GSAS-2[46].

From the volume of the perovskite unit cell V obtained by Rietveld refinement, the pseudocubic perovskite cell parameter a_P was calculated with Eq. 1.

$$a_p = \sqrt[3]{\frac{V}{4}} \qquad \text{(Eq. 1)}$$

Out of the refined mass fraction *w* of Ni, the molar amount of Ni per molar amount of perovskite *n*(Ni)/*n*(P) was calculated using Eq. 2. This is referred to as the extent of exsolution ξ.

$$\xi \equiv \frac{n\,(\mathrm{Ni})}{n\,(\mathrm{P})} = \frac{w}{1-w} \cdot \frac{M\,(\mathrm{P})}{M\,(\mathrm{Ni})} = \frac{w}{1-w} \cdot \frac{182.71\ \mathrm{g/mol}}{58.69\ \mathrm{g/mol}} \qquad \text{(Eq. 2)}$$

SEM and image analysis

High resolution SEM measurements were carried out with a JEOL JSM-6700 field emission SEM, equipped with SE and BSE detectors. For image processing the software ImageJ-win64 was used[47]. The particles were identified and measured in size with the *Analyze Particles* plugin. The average diameter size *s* was determined and for further investigation of the exsolved particles, the particle population *P* was calculated by dividing the number of identified particles through the analysed area *A*. Assuming spherical nanoparticles, the number of exsolved Ni atoms per area η_{Ni} was calculated with Eq. 3.

$$\eta_{\mathrm{Ni}} = \frac{\sum_{\mathrm{Particles}} \frac{1}{6}\pi\, s^3 \cdot \frac{\rho\,(\mathrm{Ni}) \cdot \mathrm{N_A}}{M\,(\mathrm{Ni})}}{A} = \frac{\sum_{\mathrm{Particles}} \frac{1}{6}\pi\, s^3 \cdot 91.42\ \mathrm{nm^{-3}}}{A} \qquad \text{(Eq. 3)}$$

Specific surface area measurement

Specific surface area was determined based on Kr physisorption at 77 K using an Autosorb iQ 2 (Quantachrome Instruments, Boynton Beach, Florida) apparatus and the samples were dried for 12 h before measurement. For calculation of the specific surface areas the standard Brunauer, Emmett and Teller (B.E.T.) equation was applied.

Material testing

Methane Temperature Programmed Reduction (MTPR)

In order to evaluate the reactivity of the catalysts to CH_4, MTPR experiments were carried out after oxidation. The setup included a quartz fixed-bed reactor tube (internal diameter of 6 mm) in a vertical furnace. Mass flow controllers were used to regulate the gas flow through the reactor. For testing, 150 mg of sample were used and gas flow rates were set to 50 mL min^{-1} (STP). First, the reactor was flushed with He, then the flow was changed to 5% CH_4/He. Afterwards, a heating program with a ramp of 10 °C min^{-1} was started from room temperature up to 750 °C. The exact temperature of the sample was monitored using a K-type thermocouple placed on the reactor bed. Outlet gas analysis was performed with a Hiden Analytical QGA mass spectrometer working with electron impact ionisation, a quadrupole mass filter and a secondary electron multiplier detector. The following *m/z*-values were tracked during MTPR: 2 (H_2^+), 15 (CH_3^+), 28 (CO^+), 44 (CO_2^+). To gain quantitative results, the mass spectrometer was calibrated with gas mixtures of 5% H_2/He, 5% CH_4/He, 5% CO/He and 5% CO_2/He.

Oxygen Temperature Programmed Oxidation (OTPO)

To examine the carbon deposition during MTPRs, some of them were followed by OTPO experiments in the same setup. The CO_2 production during OTPO provides insights into the coking behaviour of an oxygen carrier. For the OTPO experiments, a sample, reduced through a previous MTPR, was oxidized under a flow of 5% O_2/He. In addition to the signals for MTPR, the *m/z*-value 32 (O_2^+) was tracked and the mass spectrometer was additionally calibrated with 5% O_2/He. The heating program with a ramp of 10 °C min^{-1} was stopped when all signals reached the baseline.

Chemical looping cycling (CL) stability tests

In order to determine the stability of the material, following repeated oxidation/reduction cycles were performed in a setup that consists of a furnace in a vertical orientation, automated 4-way valves to control the gas composition being fed each time into the reactor, computer-controlled mass flow controllers (SLA5850, Brooks Instrument) that were used to regulate the flow through the system and pressure transducers (PG309-100GV, Omega) to record the system pressure. The reactor of the system is a quartz tube with internal diameter of 4 mm and 2 mm wall thickness and the local temperature was recorded with a K-type thermocouple placed in contact with the quartz reactor tube and was increased from RT to the specific experiment's temperature at a rate of 5 °C min^{-1}. The cycling was performed at 1 atm and 550 °C. The reactor was flushed with a He flow of 30 mL min^{-1} prior to commencing testing. The sample was subjected to multi-cycle isothermal reduction under 5% CH_4/He and isothermal oxidation under 5% O_2/He with inlet flow rates of 30 mL min^{-1}. Reduction and oxidation half cycles were performed for 5 min while inert gas (He) was purged through the reactor for 5 min between each half cycle in order to avoid mixing of the reducing and oxidising gases. The long-term cycling was carried out using 400 mg of sample.

Data processing

The molar fraction of all gases in the outlet $(y_x)_{outlet}$ was calculated by multiplying the calibration factor with the recorded signal minus any cracking signal from other species on that particular mass to charge ratio channel.

For the calculation of conversion, selectivity, carbon deposition and capacity, the following values were calculated.

$$N_{CO} = \int_{R} (y_{CO})_{outlet}\, \dot{n}\, dt \quad \text{(Eq. 4)}$$

$$N_{CO_2} = \int_{R} (y_{CO_2})_{outlet}\, \dot{n}\, dt \quad \text{(Eq. 5)}$$

$$N_{C} = \int_{O} (y_{CO_2})_{outlet}\, \dot{n}\, dt + \int_{O} (y_{CO})_{outlet}\, \dot{n}\, dt \quad \text{(Eq. 6)}$$

$$N_{CH_4} = \int_{R} (y_{CH_4})_{inlet}\, \dot{n}\, dt - \int_{R} (y_{CH_4})_{outlet}\, \dot{n}\, dt \quad \text{(Eq. 7)}$$

The letter under the integral denotes the reduction step (R for MTPR or reduction half-cycle) or the oxidation step (O for OTPO or oxidation half-cycle). N_{CO} and N_{CO_2} are the total moles of CO and CO_2, produced, respectively, during the reduction step. N_C is the total moles of C produced during an OPTO experiment. N_{CH_4} is the total moles of reacted CH_4. $\dot{n}$ is the total molar flow rate corresponding to each experiment.

Oxygen capacity (mol O/g of material) was calculated by:

$$\delta = (2N_{CO_2} + N_{CO}) \cdot \frac{1}{m} \quad \text{(Eq. 8)}$$

m is the sample weight used in the respective experiments.

Overall CH_4 conversion (mmol CH_4/g of material) was calculated by the following equation:

$$X^{*}_{CH_4} = (N_{CO} + N_{CO_2} + N_C) \cdot \frac{1}{m} \quad \text{(Eq. 9)}$$

m is the sample weight used in the respective experiments.

Selectivities (%) were calculated by the following equations:

$$S_{CO} = \frac{N_{CO}}{N_{CO} + N_{CO_2} + N_C} \cdot 100 \quad \text{(Eq. 10)}$$

$$S_{CO_2} = \frac{N_{CO_2}}{N_{CO} + N_{CO_2} + N_C} \cdot 100 \quad \text{(Eq. 11)}$$

$$S_C = \frac{N_C}{N_{CO} + N_{CO_2} + N_C} \cdot 100 \quad \text{(Eq. 12)}$$

Selectivity ratio was calculated by the following equation:

$$S_r = \frac{S_{CO} + S_{CO_2}}{S_C} \quad \text{(Eq. 13)}$$

Gas phase selectivity to CO (%) was calculated by the following equation:

$$S_g = \frac{N_{CO}}{N_{CO} + N_{CO_2}} \cdot 100 \quad \text{(Eq. 14)}$$

Carbon deposition (mmol C/g of material) was calculated as shown in Eq. 15, by the integration of the CO_2 curve of the TPO experiments as CO was completely absent, meaning that the carbon oxidation led only to total combustion products.

$$C_{\text{deposition}} = \frac{N_c}{m} \quad \text{(Eq. 15)}$$

m is the sample weight used in the respective experiments.

Carbon deposition* (mmol C/g of material) was calculated by carbon balance the MTPR experiments according to Eq. 16.

$$C^{*}_{\text{deposition}} = \frac{N_{\text{CH}_4} - N_{\text{CO}} - N_{\text{CO}_2}}{m} \quad \text{(Eq. 16)}$$

m is the sample weight used in the respective experiments.

FIGURES

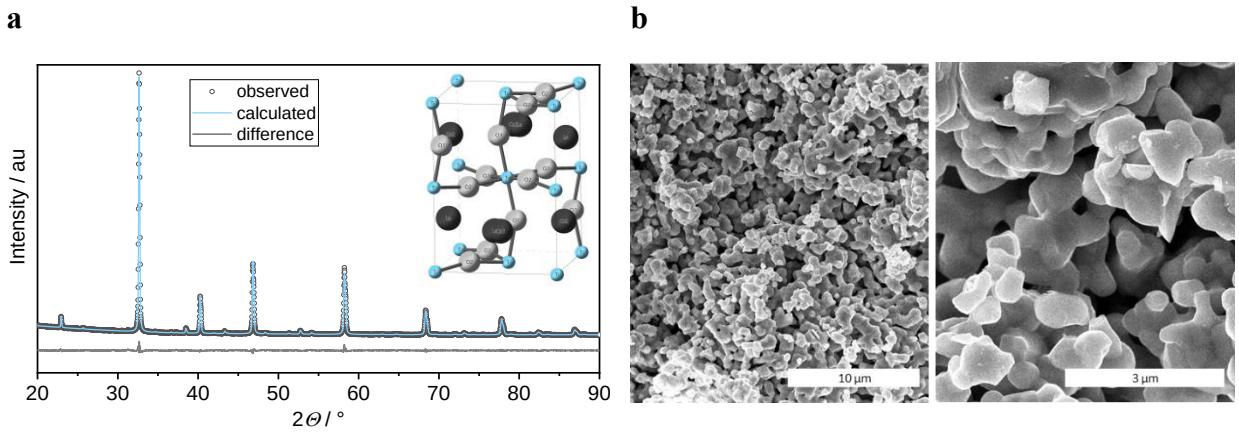

Figure 1. Structure and morphology of a porous perovskite capable of Ni exsolution. a, Rietveld refinement (*wR* 5%) of the room-temperature XRD pattern of the $La_{0.5}Ca_{0.4}Ni_{0.2}Ti_{0.8}O_{2.95}$ perovskite after sintering at 1100 °C for 12 h, with an inset of the crystal structure obtained by refinement (space group *Pnma*, individual cell parameters are a = 5.4822 Å; b = 5.4803 Å; c = 7.7594 Å and a_P = 3.8771 Å). **b**, Microstructure (SEM) of the $La_{0.5}Ca_{0.4}Ni_{0.2}Ti_{0.8}O_{2.95}$ perovskite after sintering, illustrating high porosity and homogenous grain size.

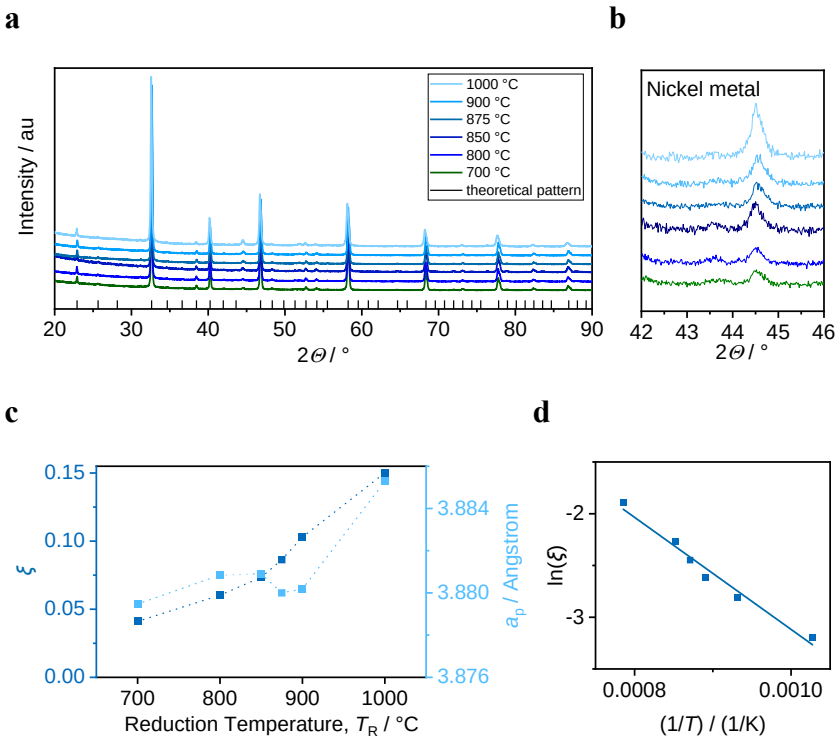

Figure 2. Controlling the extent of exsolution through the reduction temperature. a, Room-temperature XRD pattern of the $La_{0.5}Ca_{0.4}Ni_{0.2}Ti_{0.8}O_{2.95}$ perovskite after reduction in H_2 for 10 h at temperatures between 700 °C and 1000 °C. The theoretical pattern of a $Pm\bar{3}m$ perovskite double cell indicates the reflections expected for the perovskite single phase. **b**, XRD pattern detail of a reflection of the Ni phase after reduction at different temperatures **c**, Extent of exsolution ξ and pseudocubic perovskite unit cell parameter a_p with reduction/exsolution temperature **d**, Arrhenius plot of ξ versus reduction temperature.

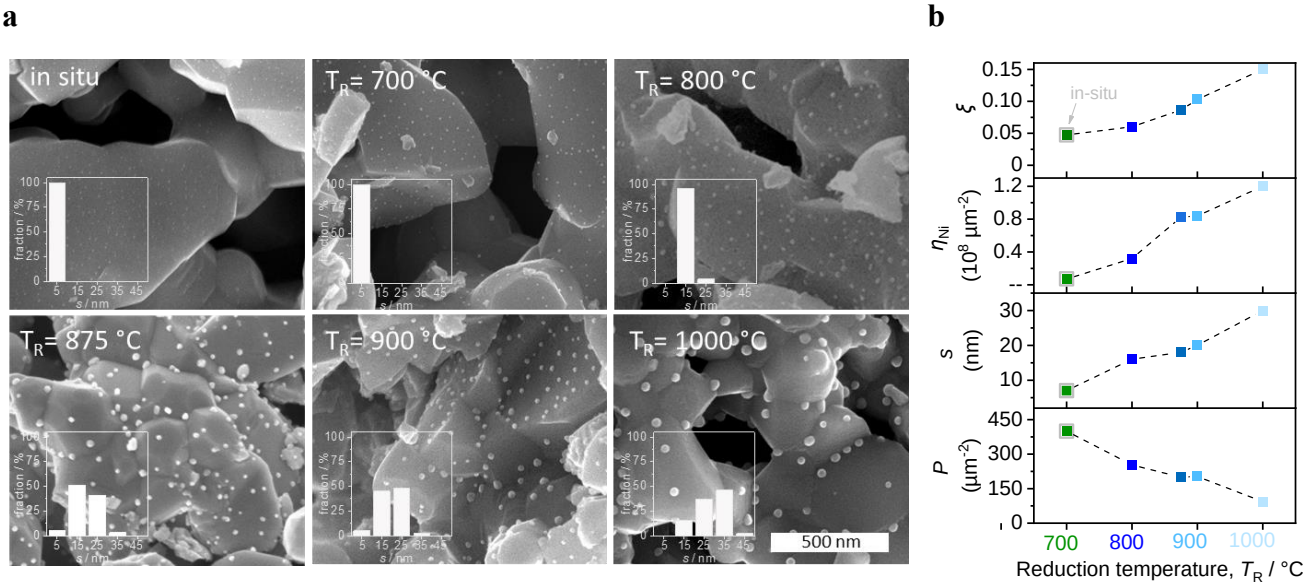

Figure 3. Controlling particle size and population through the reduction temperature. a, Micro- and Nanostructure (SEM) of the $La_{0.5}Ca_{0.4}Ni_{0.2}Ti_{0.8}O_{2.95}$ perovskite after reduction in H_2 for 10 h at temperatures (T_R) between 700 °C and 1000 °C. In situ reduction was done by heating in CH_4 up to 750 °C without additional dwell time. Reduction for 30 h at 700 °C produced very similar particle size characteristics as the 10 h one. **b**, Particle average diameter size (s), population (P) and number of exsolved Ni atoms per area (η_{Ni}) determined by SEM image analysis, as well as the extent of exsolution ξ for different reduction temperatures.

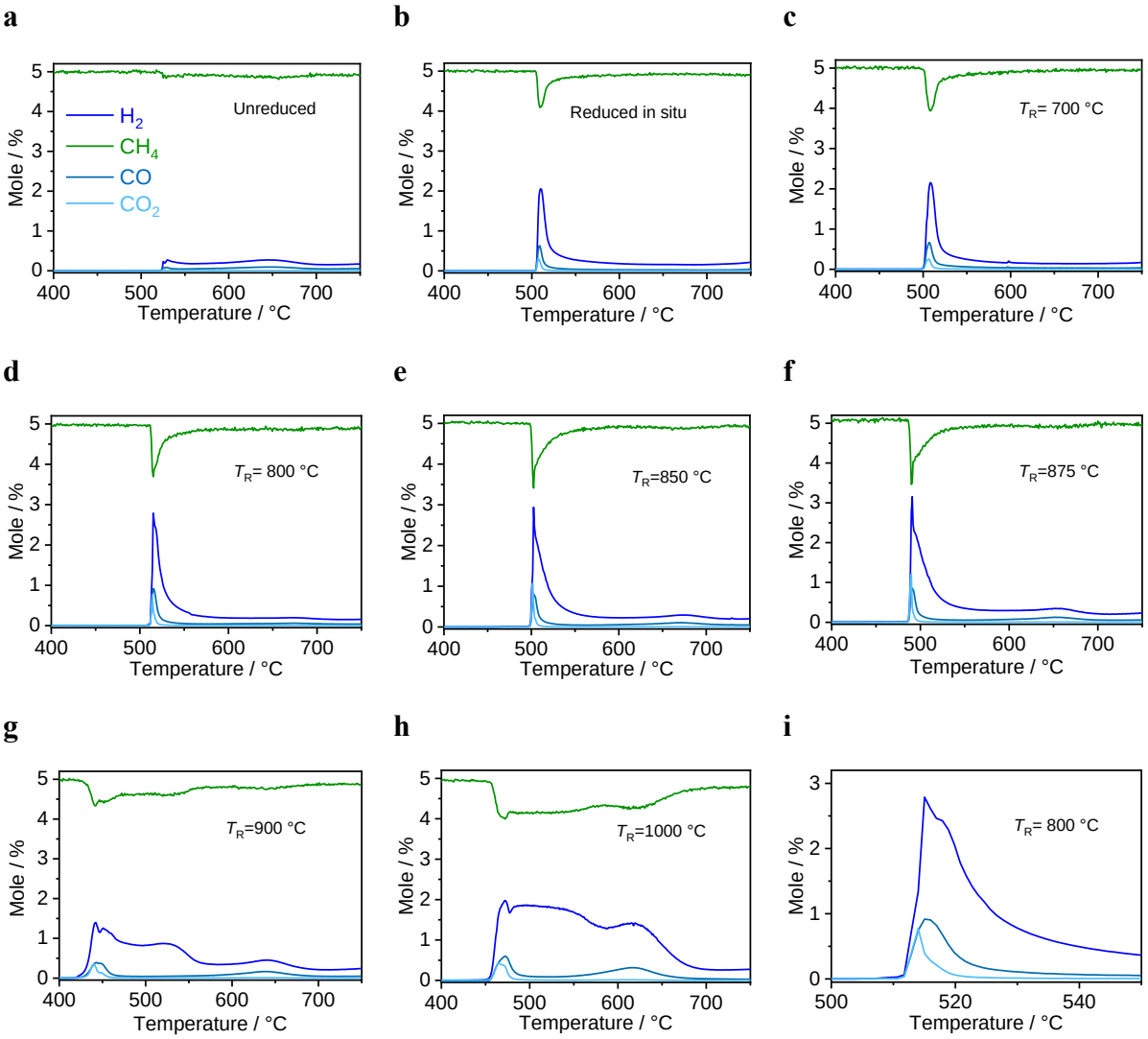

Figure 4. The effect of the extent of exsolution on CH_4 conversion. a, MTPR profile of the unreduced $La_{0.5}Ca_{0.4}Ni_{0.2}Ti_{0.8}O_{2.95}$ perovskite after sintering. The experiment resembles an in-situ reduction in CH_4, leading to the exsolution of Ni nanoparticles as showed in Fig 3. **b**, MTPR testing after oxidation of sample in a. **c-i** MTPR testing for the perovskite samples reduced in H_2 for 10 h at temperatures (T_R) between 700 °C and 1000 °C, with i being a detail of d.

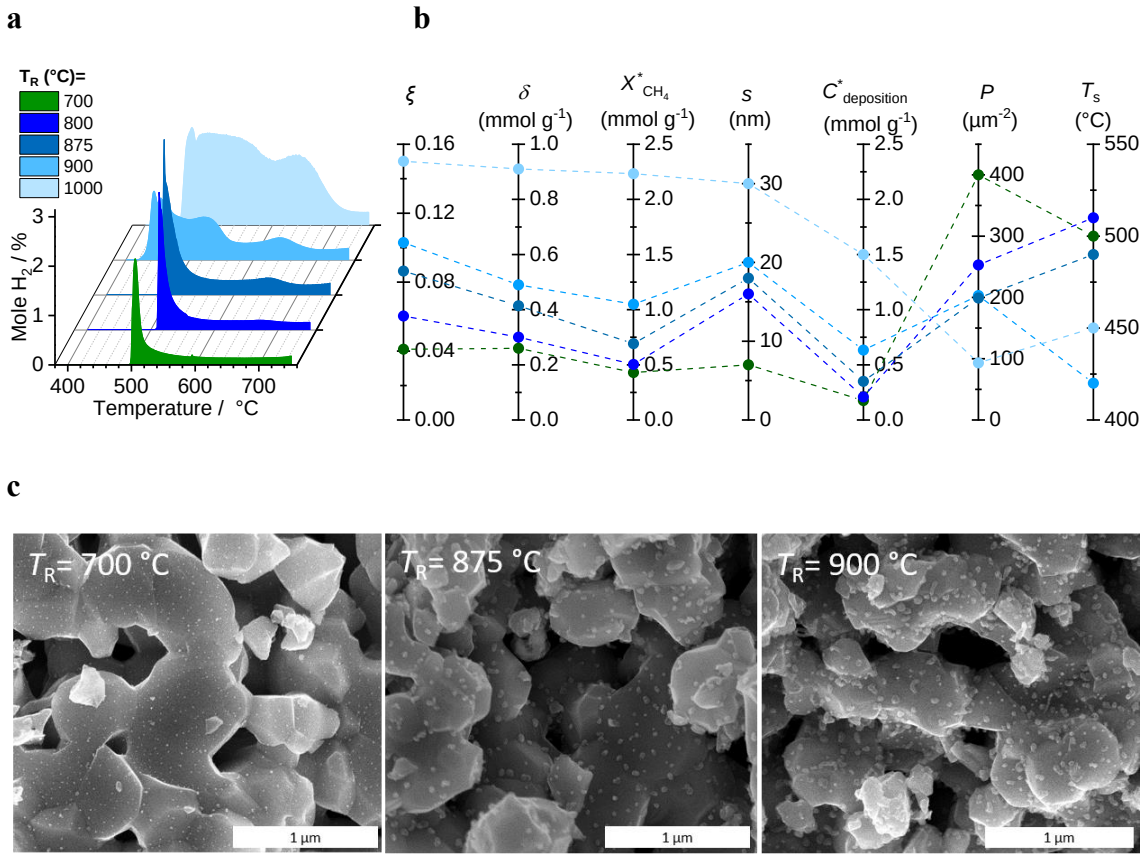

Figure 5. Correlating the characteristics of the exsolved systems with their reactivity. a, MTPR H_2 signals of the perovskite reduced at different temperatures (T_R) in H_2 for 10 h **b**, n-dimensional plot of the determined sample characteristics with ξ being the extent of exsolution, δ the oxygen capacity, X^*_{CH4} the overall CH_4 conversion, s the average particle diameter size, $C^*_{deposition}$ the carbon deposited on the samples surface during MTPR testing, P the particle population of the exsolved Ni particles and T_s the temperature of CH_4 activation. **c**, Micro- and Nanostructure of the $La_{0.5}Ca_{0.4}Ni_{0.2}Ti_{0.8}O_{2.95}$ perovskite, reduced at different temperature (T_R), after MTPR testing. The smaller nanoparticles formed at lower reduction temperature seem to be less prone for carbon fibre formation, since carbon fibres were only present at higher extent for reduction at 900 °C.

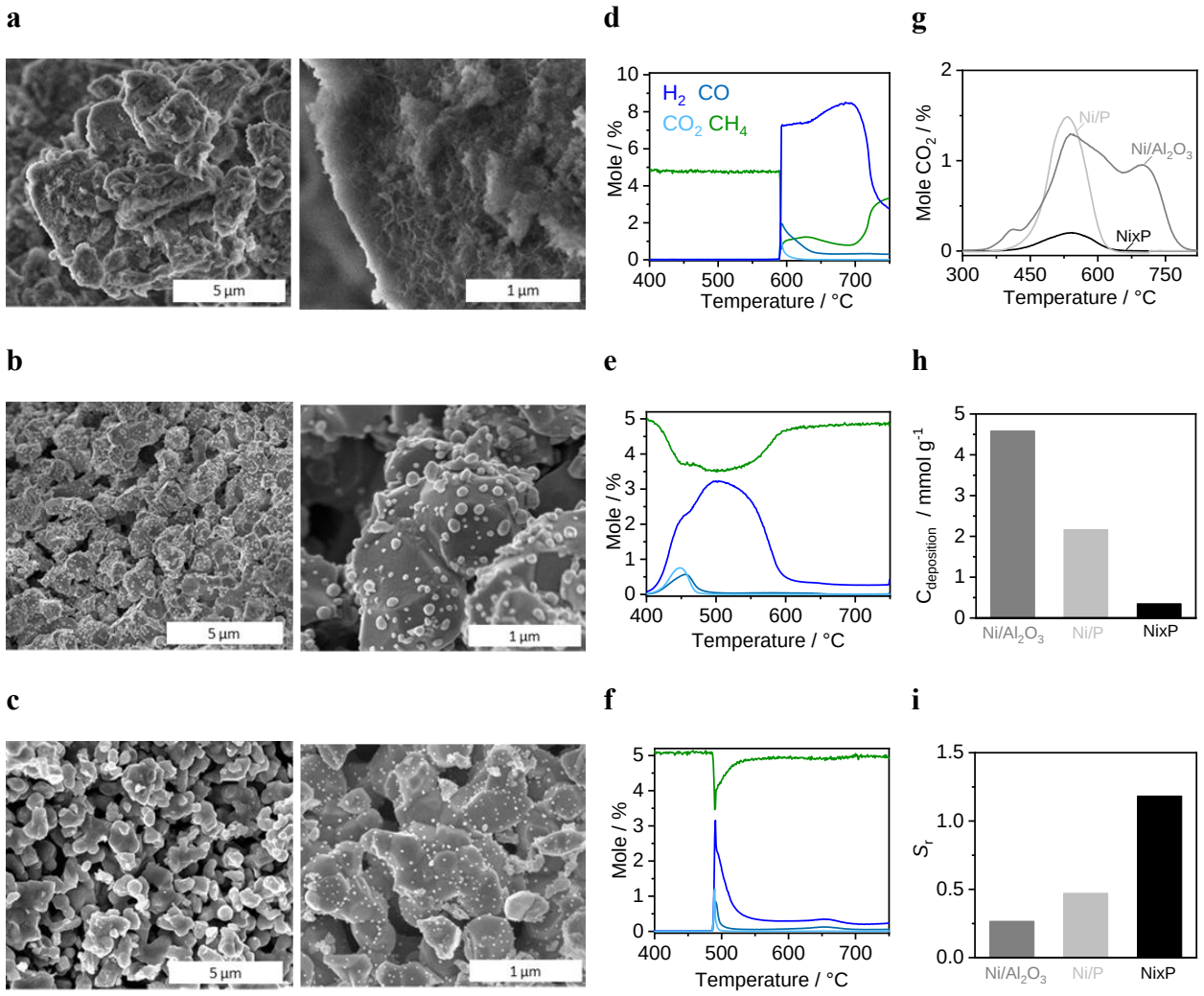

Figure 6. Comparison between exsolved and infiltrated samples. a-c, Micro- and Nanostructure (SEM) of the Ni/Al_2O_3, the Ni-infiltrated perovskite (Ni/P) and the Ni-doped perovskite after reduction at 875 °C (NixP), respectively. **d-f**, MTPR testing of the Ni/Al_2O_3, the Ni-infiltrated perovskite and the Ni-doped perovskite after reduction at 875 °C, respectively. **g**, CO_2 produced during oxidation of the samples after MTPR testing and **h**, the corresponding calculated C deposition for g **i**, Selectivity ratio S_r of oxygenated gas products (CO_x) to C deposition produced during CH_4 activation testing.

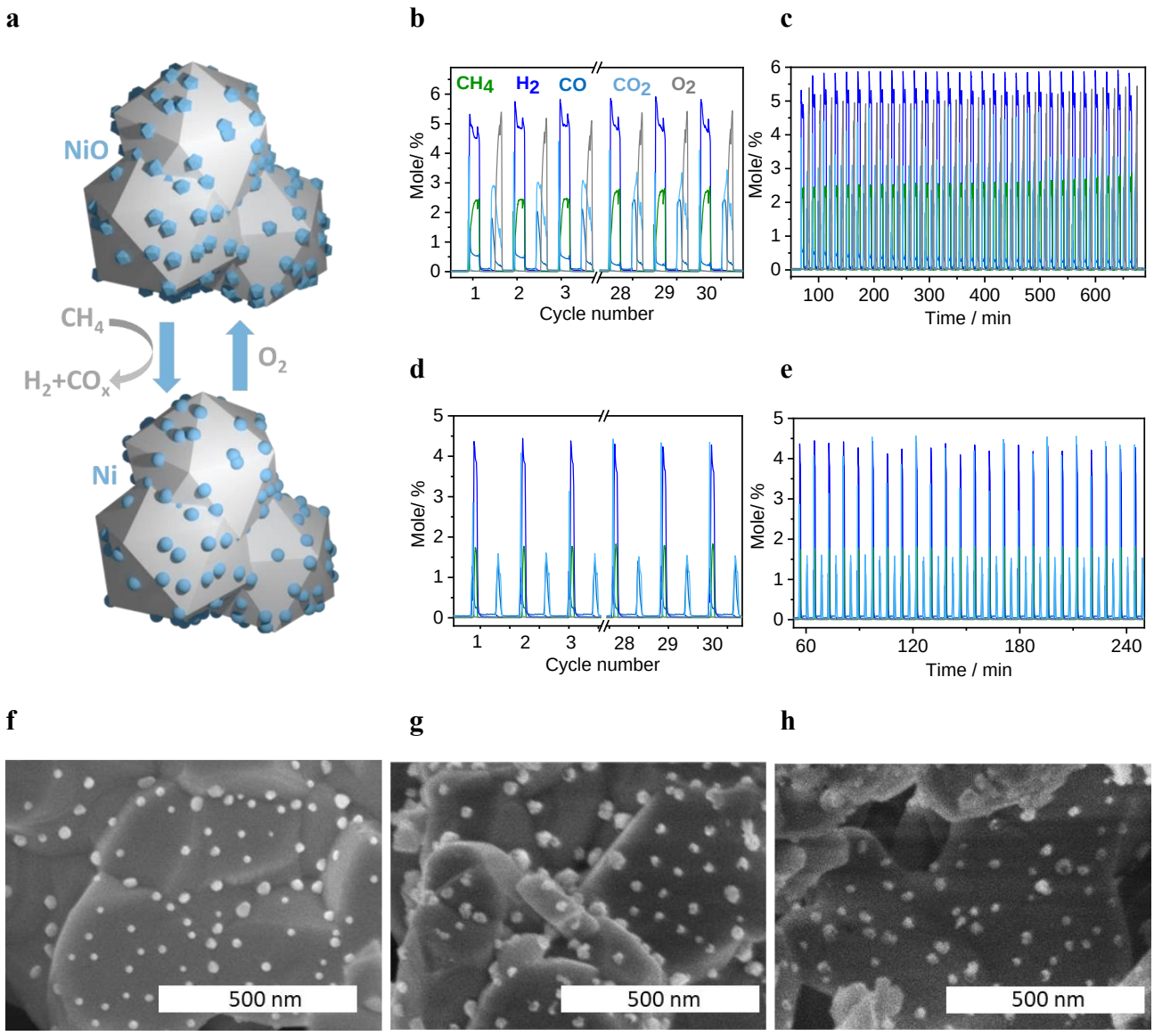

Figure 7. Long-term stability of the exsolved system in CLPO. a. Schematic illustrating the concept presented in this paper. **b.** Close up of outlet gas composition over time with cycle length of 5 min in cycles 1-3 and 28-30 **c.** Outlet gas composition over time. **d.** Close up of outlet gas composition over time with cycle length of 1 min in cycles 1-3 and 28-30 **e.** Outlet gas composition over time. Nanostructure (SEM) of the Ni-doped perovskite after **f.** Reduction at 875 °C, **g.** TPR and TPO and **h.** stability testing at 550 °C after experiments shown in b-e (60 cycles).

AUTHOR INFORMATION

Corresponding Author

*Kalliopi Kousi (kalliopi.kousi@newcastle.ac.uk).

*Dragos Neagu (dragos.neagu@newcatsle.ac.uk).

*Ian S. Metcalfe (ian.metcalfe@newcastle.ac.uk)

Funding Sources

The research leading to these results has received funding from the European Research Council under the European Union's Seventh Framework Programme (FP/2007-2013) / ERC Grant Agreement Number 320725 and from the EPSRC via grants EP/P007767/1, EP/P024807/1 and EP/R023921/1.

Data access

The data supporting this publication is available at DOI: 10.25405/data.ncl.8323601.

REFERENCES

(1) Luo, M.; Yi, Y.; Wang, S.; Wang, Z.; Du, M.; Pan, J.; Wang, Q. Review of hydrogen production using chemical-looping technology. *Renewable and Sustainable Energy Reviews* **2018**, *81*, 3186–3214, DOI: 10.1016/j.rser.2017.07.007.

(2) Posdziech, O.; Schwarze, K.; Brabandt, J. Efficient hydrogen production for industry and electricity storage via high-temperature electrolysis. *International Journal of Hydrogen Energy* **2018,** DOI: 10.1016/j.ijhydene.2018.05.169.

(3) Moghtaderi, B. Review of the Recent Chemical Looping Process Developments for Novel Energy and Fuel Applications. *Energy Fuels* **2012**, *26*, 15–40, DOI: 10.1021/ef201303d.

(4) Metcalfe, I. S.; Ray, B.; Dejoie, C.; Hu, W.; Leeuwe, C. de; Dueso, C.; García-García, F. R.; Mak, C.-M.; Papaioannou, E. I.; Thompson, C. R.; Evans, J. S. O. Overcoming chemical equilibrium limitations using a thermodynamically reversible chemical reactor. *Nature Chemistry* **2019,** DOI: 10.1038/s41557-019-0273-2.

(5) Li, K.; Wang, H.; Wei, Y. Syngas Generation from Methane Using a Chemical-Looping Concept: A Review of Oxygen Carriers. *Journal of Chemistry* **2013**, *294817*, 1–8.

(6) Wei, G.; He, F.; Huang, Z.; Zhao, K.; Zheng, A.; Li, H. Chemical-Looping Reforming of Methane Using Iron Based Oxygen Carrier Modified with Low Content Nickel. *Chin. J. Chem.* **2014**, *32*, 1271–1280, DOI: 10.1002/cjoc.201400563.

(7) Zeng, L.; Cheng, Z.; Fan, J. A.; Fan, L.-S.; Gong, J. Metal oxide redox chemistry for chemical looping processes. *Nat Rev Chem* **2018**, *2*, 349–364, DOI: 10.1038/s41570-018-0046-2.

(8) Protasova, L.; Snijkers, F. Recent developments in oxygen carrier materials for hydrogen production via chemical looping processes. *Fuel* **2016**, *181*, 75–93, DOI: 10.1016/j.fuel.2016.04.110.

(9) Tang, M.; Xu, L.; Fan, M. Progress in oxygen carrier development of methane-based chemical-looping reforming: A review. *Applied Energy* **2015**, *151*, 143–156, DOI: 10.1016/j.apenergy.2015.04.017.

(10) Johansson, M.; Mattisson, T.; Lyngfelt, A.; Abad, A. Using continuous and pulse experiments to compare two promising nickel-based oxygen carriers for use in chemical-looping technologies. *Fuel* **2008**, *87*, 988–1001, DOI: 10.1016/j.fuel.2007.08.010.

(11) Diego, L. F. de; Ortiz, M.; Adánez, J.; García-Labiano, F.; Abad, A.; Gayán, P. Synthesis gas generation by chemical-looping reforming in a batch fluidized bed reactor using Ni-based oxygen carriers. *Chemical Engineering Journal* **2008**, *144*, 289–298, DOI: 10.1016/j.cej.2008.06.004.

(12) Yentekakis, I. V.; Goula, G.; Hatzisymeon, M.; Betsi-Argyropoulou, I.; Botzolaki, G.; Kousi, K.; Kondarides, D. I.; Taylor, M. J.; Parlett, C. M.A.; Osatiashtiani, A. ; Kyriakou, G.; Holgado, J. P.; Lambert, R. M. Effect of support oxygen storage capacity on the catalytic performance of Rh nanoparticles for CO2 reforming of methane. *Applied Catalysis B: Environmental* **2019**, *243*, 490–501, DOI: 10.1016/j.apcatb.2018.10.048.

(13) Pröll, T.; Bolhàr-Nordenkampf, J.; Kolbitsch, P.; Hofbauer, H. Syngas and a separate nitrogen/argon stream via chemical looping reforming – A 140kW pilot plant study. *Fuel* **2010**, *89*, 1249–1256, DOI: 10.1016/j.fuel.2009.09.033.

(14) Juan-Juan, J.; Román-Martínez, M. C.; Illán-Gómez, M. J. Effect of potassium content in the activity of K-promoted Ni/Al2O3 catalysts for the dry reforming of methane. *Applied Catalysis A: General* **2006**, *301*, 9–15, DOI: 10.1016/j.apcata.2005.11.006.

(15) Zhang, Z. L.; Verykios, X. E. Carbon dioxide reforming of methane to synthesis gas over supported Ni catalysts. *Catalysis Today* **1994**, *21*, 589–595, DOI: 10.1016/0920-5861(94)80183-5.

(16) Wang, S.; Lu, G. Q. Effects of promoters on catalytic activity and carbon deposition of Ni/Al2O3 catalysts in CO2 reforming of CH4. *J. Chem. Technol. Biotechnol.* **2000**, *75*, 589–595, DOI: 10.1002/1097-4660(200007)75:7<589:AID-JCTB241>3.0.CO;2-7.

(17) Myung, J.; Neagu, D.; Miller, D. N.; Irvine, J. T. S. Switching on electrocatalytic activity in solid oxide cells. *Nature* **2016**, *537*, 528–532.

(18) Liu, S.; Liu, Q.; Luo, J.-L. Highly Stable and Efficient Catalyst with In Situ Exsolved Fe–Ni Alloy Nanospheres Socketed on an Oxygen Deficient Perovskite for Direct CO 2 Electrolysis. *ACS Catal.* **2016**, *6*, 6219–6228, DOI: 10.1021/acscatal.6b01555.

(19) Zubenko, D.; Singh, S.; Rosen, B. A. Exsolution of Re-alloy catalysts with enhanced stability for methane dry reforming. *Applied Catalysis B: Environmental* **2017**, *209*, 711–719, DOI: 10.1016/j.apcatb.2017.03.047.

(20) Wang, W.; Gan, L.; Lemmon, J. P.; Chen, F.; Irvine, J. T. S.; Xie, K. Enhanced carbon dioxide electrolysis at redox manipulated interfaces. *Nature communications* **2019**, *10*, 1550, DOI: 10.1038/s41467-019-09568-1.

(21) Neagu, D.; Oh, T.-S.; Miller, D. N.; Ménard, H.; Bukhari, S. M.; Gamble, S. R.; Gorte, R. J.; Vohs, J. M.; Irvine, J. T. S. Nano-socketed nickel particles with enhanced coking resistance grown in situ by redox exsolution. *Nature communications* **2015**, *6*, 8120, DOI: 10.1038/ncomms9120.

(22) Neagu, D.; Tsekouras, G.; Miller, D. N.; Ménard, H.; Irvine, J. T. S. *In situ* growth of nanoparticles through control of non-stoichiometry. *Nature Chemistry* **2013**, *5*, 916–923.

(23) Neagu, D.; Papaioannou, E. I.; Ramli, W. K. W.; Miller, D. N.; Murdoch, B. J.; Ménard, H.; Umar, A.; Barlow, A. J.; Cumpson, P. J.; Irvine, J. T. S.; Metcalfe, I. S. Demonstration of chemistry at a point through restructuring and catalytic activation at anchored nanoparticles. *Nature communications* **2017**, *8*, 1855, DOI: 10.1038/s41467-017-01880-y.

(24) Thalinger, R.; Gocyla, M.; Heggen, M.; Dunin-Borkowski, R.; Grünbacher, M.; Stöger-Pollach, M.; Schmidmair, D.; Klötzer, B.; Penner, S. Ni–perovskite interaction and its structural and catalytic consequences in methane steam reforming and methanation reactions. *Journal of Catalysis* **2016**, *337*, 26–35, DOI: 10.1016/j.jcat.2016.01.020.

(25) S G Adiya, Z. I.; Dupont, V.; Mahmud, T. Steam reforming of shale gas in a packed bed reactor with and without chemical looping using nickel based oxygen carrier. *International Journal of Hydrogen Energy* **2018**, *43*, 6904–6917, DOI: 10.1016/j.ijhydene.2018.02.083.

(26) Sun, Y.; Li, J.; Zeng, Y.; Amirkhiz, B. S.; Wang, M.; Behnamian, Y.; Luo, J. A-site deficient perovskite: the parent for in situ exsolution of highly active, regenerable nano-particles as SOFC anodes. *J. Mater. Chem. A* **2015**, *3*, 11048–11056, DOI: 10.1039/C5TA01733E.

(27) Connor, P. A.; Yue, X.; Savaniu, C. d.; Price, R.; Triantafyllou, G.; Cassidy, M.; Kerherve, G.; Payne, D. J.; Maher, R. C.; Cohen, L. F.; Tomov, R. I; Glowacki, B. A; Kumar, R. V; Irvine, J. T. S. Tailoring SOFC Electrode Microstructures for Improved Performance. *Adv. Energy Mater.* **2018**, *8*, 1800120, DOI: 10.1002/aenm.201800120.

(28) Toby, B. H. R factors in Rietveld analysis: How good is good enough? *Powder Diffr.* **2006**, *21*, 67–70, DOI: 10.1154/1.2179804.

(29) Itoh, J.; Yashima, I.; Ohashi, N.; Sakaguchi, I.; Haneda, H.; Tanaka, J. Ni Ion Diffusion in Barium Titanate Perovskite. *Nippon Seramikkusu Kyokai gakujutsu ronbunshi* **2001**, *109*, 955–959, DOI: 10.2109/jcersj.109.1275_955.

(30) Mayeshiba, T.; Morgan, D. Factors controlling oxygen migration barriers in perovskites. *Solid State Ionics* **2016**, *296*, 71–77, DOI: 10.1016/j.ssi.2016.09.007.

(31) Souza, R. A. de; Islam, M. S.; Ivers-Tiffée, E. Formation and migration of cation defects in the perovskite oxide LaMnO3. *J. Mater. Chem.* **1999**, *9*, 1621–1627, DOI: 10.1039/a901512d.

(32) *Neagu, D.; Irvine, J. T. S. Perovskite Defect Chemistry as Exemplified by Strontium Titanate. In Comprehensive inorganic chemistry II: From elements to applications, 2. ed.; Reedijk, J., Ed.; Elsevier: Amsterdam, 2013; pp 397–415*.

(33) Shannon, R. D. Revised effective ionic radii and systematic studies of interatomic distances in halides and chalcogenides. *Acta Crystallographica Section A* **1976**, *32*, 751–767, DOI: 10.1107/S0567739476001551.

(34) Neagu, D. Materials and Microstructures for High Temperature Electrochemical Devices through Control of Perovskite Defect Chemistry. *PhD Thesis at the University of St Andrews* **2012**.

(35) Wallace, W. T.; Min, B. K.; Goodman, D. W. The nucleation, growth, and stability of oxide-supported metal clusters. *Top Catal* **2005**, *34*, 17–30, DOI: 10.1007/s11244-005-3786-4.

(36) Gao, Y.; Chen, D.; Saccoccio, M.; Lu, Z.; Ciucci, F. From Material Design to Mechanism Study: Nanoscale Ni Exsolution on a Highly Active A-Site Deficient Anode Material for Solid Oxide Fuel Cells. *Nano Energy* **2016**, *27*, 499.

(37) Zheng, Y.; Li, K.; Wang, H.; Tian, D.; Wang, Y.; Zhu, X.; Wei, Y.; Zheng, M.; Luo, Y. Designed oxygen carriers from macroporous LaFeO 3 supported CeO 2 for chemical-looping reforming of methane. *Applied Catalysis B: Environmental* **2017**, *202*, 51–63, DOI: 10.1016/j.apcatb.2016.08.024.

(38) Johansson, T.; Pakhare, D.; Haynes, D.; Abdelsayed, V.; Shekhawat, D.; Spivey, J. Characterization of LaRhO3 perovskites for dry (CO2) reforming of methane (DRM). *Chemical Papers* **2014**, *68*, 117, DOI: 10.2478/s11696-014-0566-2.

(39) Choudhary, T. V.; Choudhary, V. R. Energy-efficient syngas production through catalytic oxy-methane reforming reactions. *Angewandte Chemie (International ed. in English)* **2008**, *47*, 1828–1847, DOI: 10.1002/anie.200701237.

(40) Bartholomew, C. H. Mechanisms of Nickel Catalyst Poisoning. In *Catalyst deactivation 1987: 4th International symposium : Papers*; Delmon, B., Froment, G. F., Eds.; Studies in Surface Science and Catalysis; Elsevier: Amsterdam, 1987; pp 81–104.

(41) Papadopoulou, C.; Matralis, H.; Verykios, X. *Catalysis for Alternative Energy Generation: Utilization of Biogas as a Renewable Carbon Source: Dry Reforming of Methane*, 2012.

(42) Kitiyanan, B.; Alvarez, W. E.; Harwell, J. H.; Resasco, D. E. Controlled production of single-wall carbon nanotubes by catalytic decomposition of CO on bimetallic Co–Mo catalysts. *Chemical Physics Letters* **2000**, *317*, 497–503, DOI: 10.1016/S0009-2614(99)01379-2.

(43) Chen, L.; Lu, Y.; Hong, Q.; Lin, J.; Dautzenberg, F. M. Catalytic partial oxidation of methane to syngas over Ca-decorated-Al2O3-supported Ni and NiB catalysts. *Applied Catalysis A: General* **2005**, *292*, 295–304, DOI: 10.1016/j.apcata.2005.06.010.

(44) Fan, M.-S.; Abdullah, A. Z.; Bhatia, S. Catalytic Technology for Carbon Dioxide Reforming of Methane to Synthesis Gas. *ChemCatChem* **2009**, *1*, 192–208, DOI: 10.1002/cctc.200900025.

(45) Djaidja, A.; Libs, S.; Kiennemann, A.; Barama, A. Characterization and activity in dry reforming of methane on NiMg/Al and Ni/MgO catalysts. *Catalysis Today* **2006**, *113*, 194–200, DOI: 10.1016/j.cattod.2005.11.066.

(46) Toby, B. H.; Dreele, R. B. von. GSAS-II : the genesis of a modern open-source all purpose crystallography software package. *Journal of Applied Crystallography* **2013**, *46*, 544–549, DOI: 10.1107/S0021889813003531.

(47) Rueden, C. T.; Schindelin, J.; Hiner, M. C.; DeZonia, B. E.; Walter, A. E.; Arena, E. T.; Eliceiri, K. W. ImageJ2: ImageJ for the next generation of scientific image data. *BMC bioinformatics* **2017**, *18*, 529, DOI: 10.1186/s12859-017-1934-z.

Table of Contents artwork